Applied Materials Today 50 (2026) 103240

Contents lists available at ScienceDirect

Applied Materials Today

journal homepage: www.elsevier.com/locate/apmt

Multi-material interface printing of a magneto-responsive hydrogel scaffold with tuned stiffness

E. Cinar San Segundo [1], L.B. Kunkels [1], S. Safarloo, L. van Zanten, L.E. Fratila-Apachitei, A.A. Zadpoor, M.J. Mirzaali [*]

Department of Biomechanical Engineering, Faculty of Mechanical Engineering, Delft University of Technology (TU Delft), Mekelweg 2, Delft 2628 CD, the Netherlands

ARTICLE INFO

Keywords:
Biomaterials
Magnetic hydrogel
Gelatin
Alginate
Hard-soft interfaces
Multi-material 3D printing

ABSTRACT

Osteochondral tissue engineering remains a significant challenge due to the complex biochemical and mechanical gradients between cartilage and subchondral bone. In this study, we present the development of a 3D-printed, multi-material magnetic hydrogel scaffold with tunable stiffness. To achieve this, we formulated a gelatin-alginate hydrogel matrix with various levels of embedded iron oxide magnetic particles (MPs) to create controlled hard-soft interfacial regions. The optimal composition (i.e., 2.5% gelatin, 5% alginate, and 10% (w/v) MPs) demonstrated magnetorheological behavior, including increased effective Young's modulus from 159 to 172 kPa and decreased viscosity from 175 to 145 kPa·s under a static magnetic field. Later, we evaluated scaffold printability through filament collapse, fusion, and porous scaffold tests, identifying a Gel:Alg ratio of 1:2 as optimal for structural fidelity. Mechanical and rheological characterizations confirmed that MPs significantly enhanced stiffness and responsiveness to magnetic fields. A checkered scaffold design enabled the fabrication of alternating hard and soft regions, and a bi-layered scaffold demonstrated improved interfacial adhesion. Micro-computed tomography provided quantitative evidence of magnetic field-induced particle redistribution within the hydrogel, confirming internal reorganization beyond bulk mechanical response. Importantly, in vitro live/dead assays confirmed that scaffold fabrication and magnetic functionality did not adversely affect cell viability. This platform offers a tunable, bioactive, and magneto-responsive scaffold architecture with potential for osteochondral repair or other applications requiring dynamic interface tissue engineering.

1. Introduction

Osteochondral tissue regeneration remains a significant clinical challenge due to the avascular nature of cartilage and the complex, gradient-based structure of the osteochondral unit, which exhibits variations in cell density, biochemical composition, and mechanical properties across its depth [1]. From the articular cartilage surface to the subchondral bone, factors such as chondrocyte density [2], mechanical stiffness (e.g., compressive strength and Young's modulus), hydroxyapatite concentration, and collagen type I content progressively increase. In contrast, properties such as water content [3], hydrostatic pressure, viscous modulus, and collagen type II content decrease (Fig. 1) [4]. This intricate balance ensures the functional integration of cartilage and bone. Thus, any disruption caused by trauma, degenerative diseases, or malignancies can impair joint function, leading to chronic pain and conditions such as osteoarthritis (OA) [5].

Current clinical strategies for treating extensive osteochondral defects include autologous chondrocyte implantation and osteochondral allograft transplantation [6]. While effective, these methods are constrained by donor site morbidity, immune rejection risks, and long waiting times. In response, tissue engineering approaches have emerged as promising alternatives, aiming to replicate the osteochondral interface both structurally and functionally [6]. These approaches frequently involve the use of mesenchymal stem cells (MSCs), which have the potential to differentiate into chondrocytes or osteoblasts under appropriate biochemical and mechanical cues [7–9].

To replicate the native osteochondral gradient, various scaffold architectures have been proposed, including bi-layered [10,11], tri-layered [12,13], and continuous gradient structures [14,15]. However, the simultaneous differentiation of MSCs into chondrocytes and osteoblasts within a single scaffold, while maintaining native-like structural and mechanical properties and ensuring stable adhesion

* Corresponding author.
E-mail address: m.j.mirzaali@tudelft.nl (M.J. Mirzaali).
[1] These authors contributed equally to this work

https://doi.org/10.1016/j.apmt.2026.103240
Received 1 August 2025; Received in revised form 13 April 2026; Accepted 16 April 2026
Available online 20 April 2026

between layers, remains a significant challenge [8].

Hydrogels are particularly attractive scaffold biomaterials due to their tunable three-dimensional (3D) polymer networks and high water content, which closely mimic the extracellular matrix (ECM) of soft tissues [16]. Recently, the incorporation of magnetic particles (MPs) into hydrogels has enabled the development of magneto-responsive hydrogels with tunable rheological properties under external magnetic fields [17,18]. This approach allows for non-contact mechanical stimulation, offering a novel strategy to direct cell behavior within a controlled microenvironment.

Magnetic hydrogels have been utilized in cartilage and bone tissue engineering to guide fiber alignment in bi-layered scaffolds [19], provide mechanical stimulation [20,21], and promote MSC differentiation in single-layered systems [22,23]. Most of these systems have relied on alginate and methylcellulose as the base hydrogel biomaterials. However, gelatin, a denatured form of collagen containing the RGD (Arg--Gly-Asp) motif, provides enhanced support for cell adhesion, proliferation, and differentiation, especially relevant for the bone side of the interface [24].

In this study, we demonstrate the 3D printing of a magneto responsive, multi-material hydrogel scaffold using a dual-nozzle extrusion setup. The two nozzles extrude a gelatin-alginate hydrogel with and without embedded MPs, enabling the spatial patterning of magnetically active and passive regions in a checkerboard configuration. This architecture aims to create localized zones with tunable mechanical properties under a magnetic field while enhancing interfacial adhesion between layers in future multi-layer scaffold designs. The proposed structure serves as a modular platform for the development of next-generation osteochondral scaffolds, mimicking both the biochemical and mechanical gradients of native tissue.

2. Materials and methods

2.1. Biomaterials

The following materials were used as received: sodium alginate (ALG, powder, CAS No. 9005–38−3), gelatin from porcine skin (GEL, powder, Type A, 300 g Bloom, CAS No. 9000–70−8), iron(II,III) oxide magnetic particles (MPs, <5 μm, 95% purity, M_w 231.53, CAS No. 1317–61−9), phosphate-buffered saline (PBS, pH 7.4), and calcium chloride dihydrate ($CaCl_2{\cdot}2H_2O$, ≥ 99.0% purity, M_w 147.01, CAS No. 10035–04−8). All reagents were purchased from Sigma-Aldrich.

2.2. Magnetic hydrogel ink preparation

Hydrogel inks were prepared by dissolving GEL and ALG powders in PBS under mechanical stirring (100–300 rpm) at 40 °C for 45 min. The solutions were then transferred to syringes, i.e., a step during which most air bubbles were introduced, followed by centrifugation (1400 rpm, 5 min, 23 °C) to remove these bubbles. These centrifugation conditions were sufficient to promote the migration of air bubbles while preserving any visible phase separation of sedimentation of the polymer components. Three Gel:Alg ratios were formulated: 5%:5% (1:1), 5%:2.5% (2:1), and 2.5%:5% (1:2) by weight.

Pre-crosslinking was performed using $CaCl_2$ solutions: 50 mM for the 1:1 and 1:2 hydrogels, and 25 mM for the 2:1 formulation, with a $CaCl_2$-to-PBS volume ratio of 1:3. The solutions were loaded into Luer-lock syringes for controlled mixing. For magnetic formulations, $CaCl_2$ solutions were first mixed with MPs (10% and 20% w/v), dispersed by vortexing (1000 rpm, 1 min, 23 °C) followed by sonication (1 min, 23 °C). The resulting suspension was then used for pre-crosslinking. The syringes containing the crosslinker suspension were connected to the syringes containing the dissolved, pre-centrifuged gelatin-alginate polymer solution using a Luer-lock connector. Before mixing, a small amount of polymer solution was gently expelled to remove any trapped air within the connector. The solutions were then mixed by alternately transferring the contents between the two syringes for 5 min, resulting in a homogeneous dispersion while minimizing air bubble formation during crosslinking. All inks were subsequently refrigerated at 4 °C overnight to initiate partial gelation prior to printing. A summary of the process is shown in Fig. 2.

2.3. Magnetic characterization of hydrogels

Mössbauer spectroscopy. Transmission ^{57}Fe Mössbauer spectra were collected at room temperature using a sinusoidal-velocity spectrometer with a ^{57}Co(Rh) source. Velocity calibration was performed using an α-Fe foil at room temperature. The Mössbauer spectra were fitted using the Mosswinn 4.0 program [25].

Vibrating sample magnetometry (VSM) were performed using a DMS Model 10 vector VSM, which records both in-plane and out-of-plane magnetic hysteresis loops. For each sample, a small piece of material with a mass of approximately 4 mg, was cut from each sheet and weighed using a balance. The VSM signal was calibrated using a Ni foil with a thickness of 0.3 mm, dimensions of 5 mm × 5 mm, and a mass of 60.1 mg, assuming a magnetic moment of 3.3 mA·m^2 based on the specific magnetization of Ni (55.1 A·m^2/kg) [26]. The macroscopic

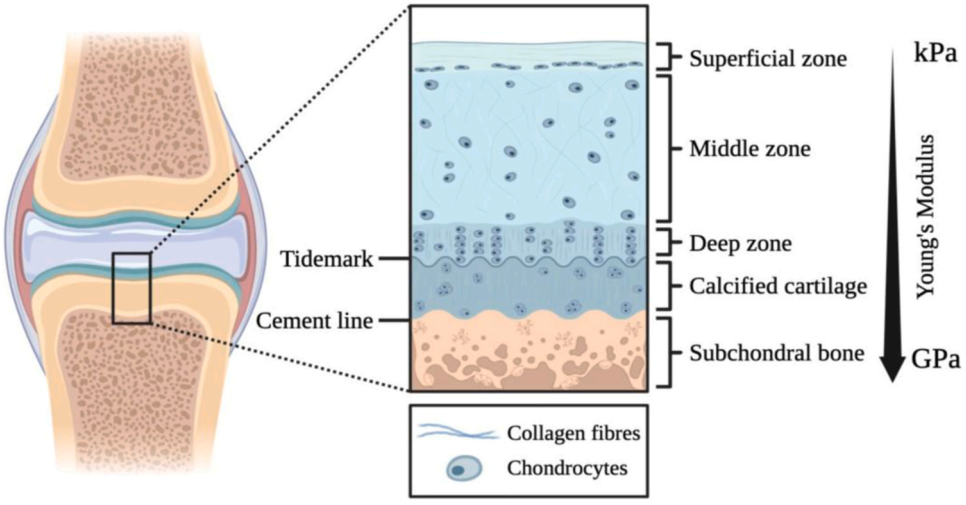

Fig. 1. A schematic representation of the osteochondral interface, illustrating the biological and mechanical gradients from the articular cartilage surface to the subchondral bone.

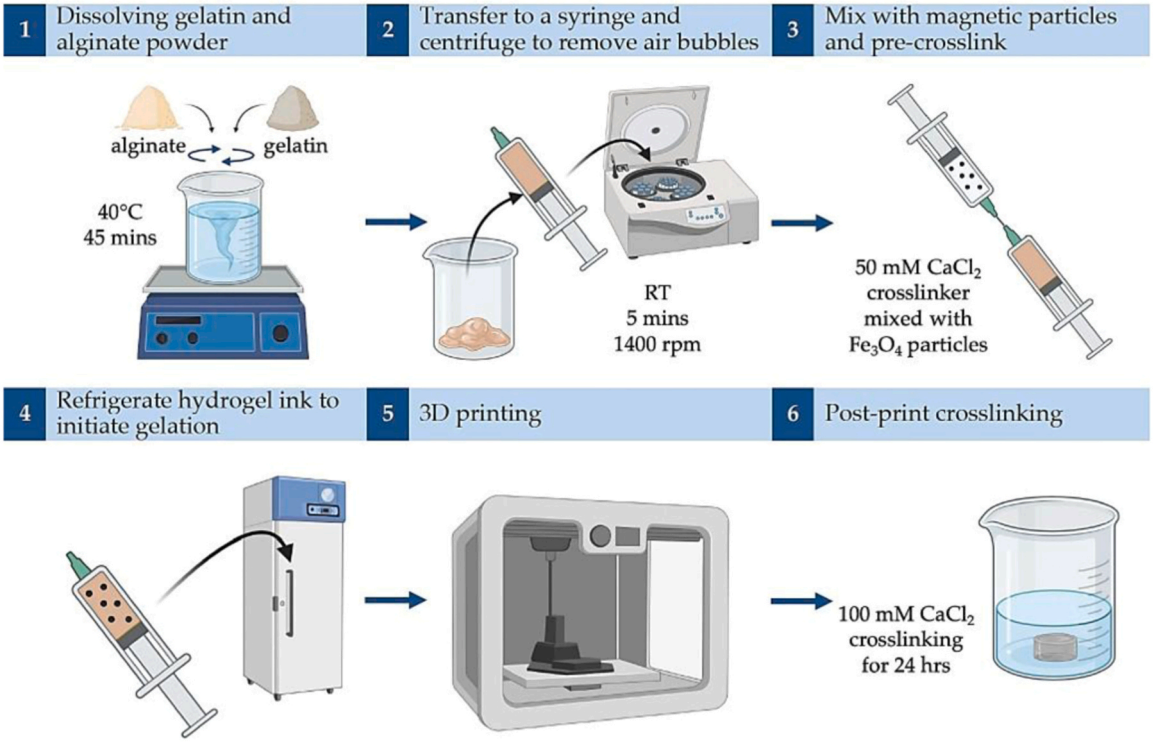

Fig. 2. A stepwise schematic representation of the preparation and 3D printing of the gelatin-alginate (Gel:Alg) magnetic hydrogel ink. Stage 1: Dissolution of GEL and ALG powders in PBS under continuous stirring at 40 °C; Stage 2: Transfer to a syringe and removal of air bubbles via centrifugation; Stage 3: Mixing with 50 mM $CaCl_2$ and magnetic particle solution; Stage 4: Gelation initiation by overnight storage at 4 °C; Stage 5: 3D printing of the hydrogel; Stage 6: Post-printing crosslinking in 100 mM $CaCl_2$.

magnetic properties of the scaffolds, including saturation magnetic moment and coercivity, were then measured at room temperature under a maximum applied field of 2 T. The background signal arising from the sample holder and vibration coupling was accounted for by measuring a control sample without magnetic particles. Finally, the measured magnetic moments were normalized by the sample mass to calculate the specific magnetization in $A{\cdot}m^2/kg$.

2.4. Hydrogel ink printability evaluation

Printing parameters. Prior to printing, pre-crosslinked hydrogel inks were equilibrated to room temperature. All specimens were printed using a BioScaffolder 3.1 (GeSiM, Germany) with 410 μm conical nozzle tips (VIEWEG GmbH, Germany). The printing experiments were conducted at 23°C, controlled using a room thermostat, with both the nozzle and print bed maintained at ambient temperature and humidity (i.e., non-heated configuration). Printing conditions were as follows: 2 mm/s print speed, 0.80 s start and end break times, 5.00 mm/s vertical tear-off speed, and 2.00 mm vertical tear-off distance. Extrusion pressure was optimized for each ink composition to ensure continuous flow and avoid nozzle clogging.

Filament fusion and collapse tests. To assess structural fidelity, filament fusion and collapse tests were performed as described by Ribeiro *et al.* [27]. For the filament collapse test, hydrogel strands were extruded over polylactic acid (PLA) supports with increasing intercolumn distances (1.0, 2.0, 4.0, 8.0, and 16.0 mm), and deflection angles were measured. For the filament fusion test, three-layer scaffolds were printed with varying interstrand distances (0.50–2.00 mm, in 0.05 mm increments). Filament widths and inter-filament gaps were measured for each configuration.

Porous scaffold fabrication. To evaluate printability and shape retention, four-layer square scaffolds ($12 \times 12 \times 2$ mm^3) were printed using various Gel:Alg:MP compositions with 1 or 2 mm strand spacing and alternating 90° layer orientations. All specimens were imaged in HEIC format using a handheld digital microscope (AmScope UTP Series, United States) and analyzed using ImageJ (version 1.53a, U. S. National Institutes of Health, United States). Each test was performed in triplicate ($n = 3$).

2.5. Magnetic scaffold fabrication

Two scaffold designs were fabricated: a single-material scaffold for preliminary mechanical and rheological characterization of each hydrogel composition, and a multi-material scaffold as a proof-of-concept for osteochondral interface mimicry by combining the hydrogel with and without MPs as the dual-component material.

Single-material scaffolds were manually extruded using 410 μm nozzle and 5 mL syringe to create four-layer structures with a 10×10 mm^2 base (Fig. 3a) with compositions of Gel:Alg:MP of 1:2:0, and 1:2:10. Following printing, scaffolds were crosslinked in 100 mM $CaCl_2$ solution for 24 h. Surface topography and MP distribution were evaluated using a 3D optical profilometer (Profilm3D, Filmetrics, United States) immediately after applying a magnetic field for 30 min and again one hour after magnet removal.

Multi-material scaffolds featured a checkered architecture comprising alternating soft and hard hydrogel sections printed using the BioScaffolder 3.1 (GeSiM, Germany) with the same printing parameters as outlined in Section 2.4. Soft regions consisted of Gel:Alg hydrogels without MPs, while hard regions incorporated embedded MPs at concentrations of 10 or 20% (w/v). The final structure measured $10.4 \times 7.2 \times 2.0$ mm^3 , with unit cells of $4.0 \times 4.0 \times 2.0$ mm^3 (Fig. 3b). This configuration allowed investigation of local mechanical contrast and interfacial compatibility under magnetic stimulation.

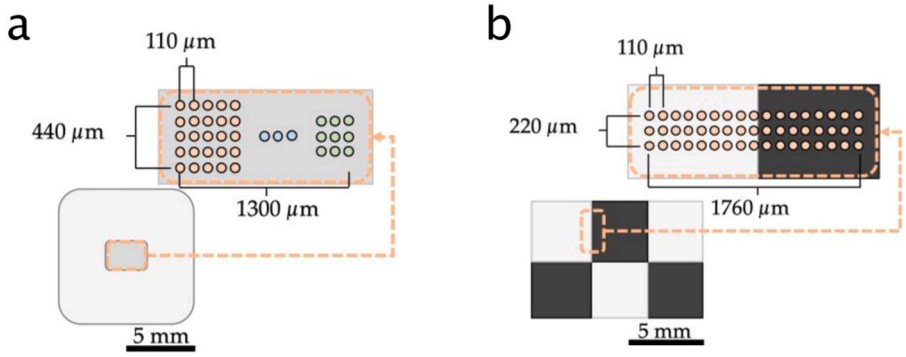

Fig. 3. (a) A schematic drawing of nanoindentation test point distribution for single-material scaffolds (10 × 10 × 2 mm^3), with 5 × 5 points for quasi-static testing (light orange), 3 × 1 for stress relaxation (light blue), and 3 × 3 for dynamic mechanical analysis (light green). (b) Test point configuration for multi-material scaffolds (10.4 × 7.2 × 2 mm^3), with 17 × 3 indentation points spaced 110 μm apart for interface mechanical characterization.

2.6. Micro computed tomography analysis

Micro-computed tomography (μCT) was employed to non-destructively assess the internal distribution of MPs within hydrogel specimens before and after magnetic field exposure. The hydrogel specimen was cylindrical, with a height and diameter of 4 mm. The same specimen was scanned under both conditions to enable paired comparison.

Scans were performed using a ZEISS Xradia Context scanner (Carl Zeiss AG, Germany) with an X-ray source operated at 80 kV and 87 μA, and an exposure time of 1 s per projection. A total of 3501 projections were acquired per scan, yielding reconstructed volumes with an isotropic voxel size of 2.3 μm. Following the initial scan, a magnetic field was applied beneath the sample for 30 min, after which the specimen was scanned again using identical imaging parameters.

During scanning, samples were maintained in a hydrated state and immobilized within a sealed centrifuge tube filled with water to prevent dehydration and leakage. The specimen was mechanically stabilized using a thin polymer film to prevent movement during acquisition. A physical marker on the sample holder was used to ensure consistent orientation and alignment between pre- and post-magnetization scans.

Projection images were reconstructed into cross-sectional slices using the scanner's proprietary reconstruction software (Reconstructor Scout-and-Scan Control System, v.16.2.18058). The reconstructed datasets were subsequently imported into Dragonfly software (v. 2022.1, build 1249; Object Research Systems, Canada) for region-of-interest (ROI) selection, manual global intensity thresholding, and quantitative analysis. The ROI encompassed the full reconstructed sample volume. No image filtering or smoothing was applied. MP center-of-mass coordinates were extracted, and their spatial distributions along the vertical axis (parallel to the direction of magnetic field application) were analyzed to evaluate particle redistribution following magnetic field application.

2.7. Mechanical and rheological characterization

2.7.1. Nanoindentation testing (quasi-static, viscoelastic, and dynamic)

Mechanical behavior was assessed using a nanoindenter (Piuma, Optics11 BV, The Netherlands). The quasi-static compression tests were performed using a strain rate: 0.5 s^{-1}, approach speed: 1.5 μm/s, indentation depth: 3 μm, and holding time: 1 s. The effective Young's moduli were calculated using the Hertz model [28], based on fitting the model on the initial slope (corresponding to 1–5% strain) of the loading portion of the load-indentation curves.

During the stress relaxation tests, to simulate an instantaneous indentation, a high indentation velocity of 5 μm/s to a depth of approximately 5 μm was applied and maintained for 300 s (Fig. S1a of the supplementary document). The creep tests were conducted with an indentation speed of 5 μN/s until the indentation depth corresponding to 5 μN was reached and held for a duration of 300 s (Fig. S1b of the supplementary document). Moreover, following the manufacturer's guidelines for optimal DMA data acquisition, the frequency sweep tests were conducted at four frequencies (1, 2, 4, and 10 Hz) with small amplitudes of 200 nm and an indentation depth of 3 μm. This ensured that, as recommended, $h_0/h << 0.25$, where h_0 is the amplitude and h is the indentation depth. Before starting the frequency sweep at the pre-determined depth, the hydrogel was indented to the necessary depth and allowed to reach full relaxation using the time from the previously conducted stress relaxation tests on the test samples of Gel:Alg:MP 1:2:0 and 1:2:10 before applying the dynamic oscillatory tests.

2.7.2. Magnetic field exposure during indentation

Hydrogel specimens were immersed in the 100 mM $CaCl_2$ cross-linking solution for 24 h and tested in the presence and absence of a uniaxial magnetic field (Fig. 4). A neodymium magnet (20 × 10 mm, Webcraft GmbH, Germany) was placed beneath the Petri dish containing the multi-material scaffolds for 30 min and Young's Moduli were evaluated. According to the manufacturer, with an approximately 1 mm air gap between the neodymium magnet and the hydrogel, the magnet's pull force is approximately 59 N. Subsequently, the effects of remanent magnetization on the Young's Moduli were also evaluated one hour post magnet removal.

2.7.3. Nanoindentation probe geometry and material parameters

Indentation probes consisted of a glass sphere (radius: 51 μm) mounted on a borosilicate cantilever with a stiffness of 4.21 N/m, and a single-mode optical fiber for precise detection of cantilever deflection. The probes were selected according to manufacturer guidelines based on hydrogel stiffness, particle size, and surface roughness [29,30]. A Poisson's ratio (ν) of 0.45 was assumed, with reported values for hydrated polymer networks such as polyacrylamide gels and PDMS elastomers, which typically range between 0.25 and 0.49 depending on crosslinking density and solvent flow effects [31] and [32]. Highly crosslinked hydrogel formulations often exhibit ν values approaching 0.45, reflecting slight compressibility below the incompressible limit of 0.5 due to network porosity and fluid redistribution.

2.7.4. Tensile integrity testing of biphasic hydrogel structures

Interfacial integrity between magnetic and non-magnetic hydrogel regions was assessed through uniaxial tensile testing using a mechanical testing machine (LR-5K, Lloyd Instruments Ltd., UK) equipped with a 50 N load cell. Dogbone-shaped specimens (adapted from ASTM D412–16 specifications [33]) were fabricated using a custom mold (Fig. S2 of the supplementary document). The mold featured a defined neck region with a width of 10 mm, a thickness of 5 mm, and a gauge length of 45 mm. For biphasic specimens, a defined volume of magnetic

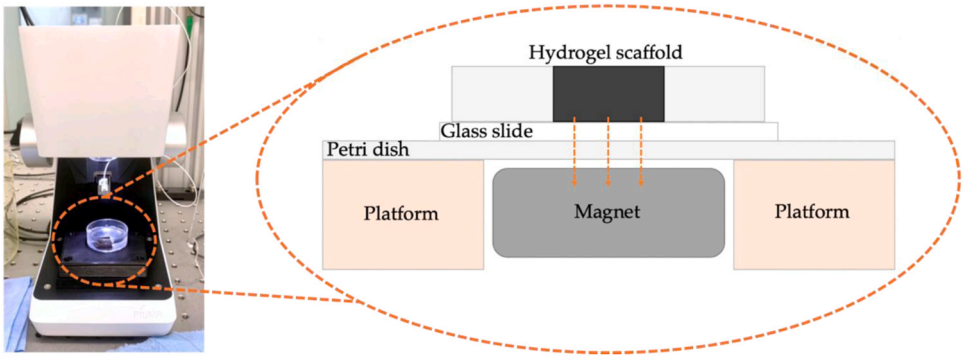

Fig. 4. Nanoindentation setup with the custom 3D-printed platform containing an embedded neodymium magnet, used to expose scaffolds to a static magnetic field during mechanical testing.

hydrogel was first injected into the center of the mold, followed by non-magnetic hydrogel in the grip regions, resulting in a reproducible magnetic segment length within the gauge section.

Specimens were clamped at the grip sections using custom 3D-printed PLA grips incorporating adjustable TPU clamping plates (Fig. S3 of the supplementary document). The clamping surfaces were lined with waterproof silicon carbide sandpaper (FEPA P800) to increase friction with the hydrogel. This setup enabled secure mounting without applying a preload and prevented specimen slippage during testing. Samples were loaded in uniaxial tension at a crosshead speed of 0.25 mm/s until failure, defined as complete specimen rupture. Force and displacement were recorded for three replicates per group (n = 3).

Two groups were evaluated: (i) homogeneous dogbone specimens fabricated entirely from the non-magnetic hydrogel (Gel:Alg:MP 1:2:0) and (ii) biphasic dogbone specimens comprising non-magnetic end regions with a magnetic hydrogel neck (Gel:Alg:MP 1:2:10). For each specimen, a total hydrogel volume of 5 mL was used. In biphasic specimens, this volume consisted of 4 mL non-magnetic hydrogel and 1 mL magnetic hydrogel centered within the neck region, whereas homogeneous specimens consisted of 5 mL non-magnetic hydrogel. All the specimens were crosslinked in 100 mM $CaCl_2$ for 24 h prior to testing.

Engineering stress and strain were calculated from the cross-sectional area and gauge length of the neck region for each specimen, as measured with digital calipers. Maximum stress and strain at break were extracted from the stress-strain curves. The elastic moduli were calculated as the slope of the initial linear region of the stress-strain curve, identified using a moving linear regression with a window size of 50 data points, from which the maximum slope was extracted. Fracture locations were documented and classified as bulk failure or interfacial failure to qualitatively assess bonding between the magnetic and non-magnetic phases.

2.8. In vitro cell culture and viability

2.8.1. Cell preculture and seeding

Cytocompatibility was evaluated using mouse preosteoblasts (MC3T3-E1, Sigma-Aldrich, Germany). Cells were cultured at 37 °C and 5% CO_2 in α-minimum essential medium (α-MEM without nucleosides and L-glutamine. Pelobiotech, Germany), supplemented with L-glutamine 100 × (Pelobiotech, Germany), 10% (v/v) fetal bovine serum, and 1% (v/v) penicillin-streptomycin (Thermo Fisher Scientific, USA). The expansion medium was replaced every second day.

Prior to hydrogel preparation, the dry polymer powders were sterilized by UV exposure for 20 min. Hydrogels were then fabricated by direct casting in 48-well plates and subsequently crosslinked by immersion in 100 mM $CaCl_2$ for 45 min, yielding cylindrical constructs that filled the entire well and formed a continuous interface with the well walls (i.e., no peripheral gaps). Prior to cell seeding, constructs were immersed in 500 μL of culture medium for 1 h and equilibrated at 37 °C for 10 min. Preosteoblasts were seeded onto the hydrogel surface in droplets (5×10^4 cells/100 μL). After 4 h of incubation, additional medium was added to reach a total volume of 500 μL per well. From day 2 onwards, osteogenic culture medium, consisting of the culture medium supplemented with 50 μg/mL ascorbic acid and 4 mM β-glycerophosphate (Sigma-Aldrich, Germany), was used. Samples were cultured for up to 7 days with medium changes every 2–3 days.

All assays were performed in duplicate, and experiments were repeated twice.

2.8.2. Live/dead staining and imaging for cell viability

Cell viability was assessed using the live/dead™ Viability/Cytotoxicity Kit for Mammalian Cells (Thermo Fisher Scientific, USA). Specimens were washed three times with phosphate buffer saline (PBS) and stained using 2 μM Calcein AM and 1.5 μM Ethidium Homodimer−1 (EthD−1) at 37°C for 30 min. Samples were subsequently rinsed with PBS and imaged by fluorescence microscopy.

Live/dead imaging was performed using an upright fluorescence microscope (Nikon Eclipse LV100D-U, Nikon Corporation, Japan) equipped with a monochrome camera and interchangeable fluorescence filter cubes. Image acquisition was performed with a 10 × objective (NA= 0.30) using filter sets for calcein AM (live cells) and EthD−1 (dead cells). Each channel was recorded as a grayscale image and subsequently merged and pseudocolored in ImageJ (green: live; red: dead) for visualization. For each fluorescent channel, brightness and contrast were adjusted independently to improve signal visibility, with settings optimized for each image according to fluorescence intensity.

2.9. Statistical analysis

All statistical analyses were conducted in MATLAB (version 2024a, Mathworks, United States). One-way ANOVA was used to assess group differences, followed by Tukey-Kramer post hoc tests for pairwise comparisons. Specifically, ANOVA was applied to compare (i) shape fidelity ratios of the checkered multi-material scaffold design in the x-, y-, and z-directions across different crosslinking time points between experimental and theoretical values, and (ii) effective Young's moduli of the different hydrogel formulations. Statistical significance was defined as follows: $p < 0.05$ (*), $p < 0.01$ (**), $p < 0.001$ (***), and $p < 0.0001$ (****). All experiments were performed in triplicate ($n = 3$).

For μCT-based particle distribution analysis, changes in particle center-of-mass positions were quantified using the Kolmogorov–Smirnov distance (D_{KS}) as a measure of effect size, implemented in IBM SPSS Statistics 29 (IBM Corp., USA). To account for unequal particle counts between pre- and post-magnetization scans, the larger dataset was downsampled to match the smaller dataset prior to analysis. D_{KS} values were evaluated independently along each axis, and relative differences between axes were used to assess the directionality of particle redistribution within the scaffold.

3. Results

3.1. Magnetic characterization of hydrogels

To validate the magnetic properties and the rationale behind the selected doping ratios, Mössbauer spectroscopy and VSM were performed on the Gel:Alg:MP 1:2:10 and 1:2:20 scaffolds. The Mössbauer spectra of both samples confirmed a consistent composition, primarily consisting of magnetite (~80%) and maghemite (~20%) (Fig. S4 and Table S1 of the supplementary document). These findings confirm the ferrimagnetic nature of the dopants and indicate that the magnetic phase remained stable and uniform across different loading concentrations.

VSM analysis further quantified the magnetic response of the composite scaffolds (Figs. S5 and S6 of the supplementary document). While the hydrogel matrix without particles exhibited a negligible magnetic signal, approximately two orders of magnitude lower than that of the particle-loaded hydrogels, the MP-loaded scaffolds showed distinct magnetic behavior. The saturation magnetization values were 19 ± 1 $\mu A \cdot m^2/kg$ for the Gel:Alg:MP 1:2:10 sample and 28 ± 2 $\mu A \cdot m^2/kg$ for the 1:2:20 sample. Interestingly, the ratio of saturation magnetization between the two concentrations (1.47 ± 0.14) deviated from the theoretical doubling (ratio of 2) expected from the precursor ratios. The Gel:Alg:MP 1:2:10 sample exhibited a coercivity 50% higher than that of the 1:2:20 sample. This suggests that, at higher loading, magnetic interactions or particle coagulation may influence the magnetic reversal behavior, whereas the Gel:Alg:MP 1:2:10 sample maintains a higher resistance to demagnetization. Furthermore, high-field fitting of the 2 T curves revealed a positive slope for both samples, particularly in the Gel:Alg:MP 1:2:20 sample (0.44 ± 0.03 $\mu A \cdot m^2/T$), suggesting the presence of a minor paramagnetic fraction. Finally, the Gel:Alg:MP 1:2:10 ratio provided a more efficient magnetic response per unit mass of dopant than the Gel:Alg:MP 1:2:20 sample.

3.2. Magnetic hydrogel printability

Printing parameters. Hydrogel compositions with higher gelatin concentrations required increased extrusion pressure during the printing process. In particular, the Gel:Alg:MP ratios of 1:1:0, 2:1:0, and 1:2:0 required 100, 60, and 45 kPa, respectively. The inclusion of MPs in the 1:2:0 formulation further increased the required pressure to 60 kPa (1:2:10) and 70 kPa (1:2:20). Despite these adjustments, smooth and continuous extrusion was most consistently achieved with the 1:2:0-based formulations.

Filament collapse and fusion tests. Filament collapse tests demonstrated that hydrogels with higher gelatin content (Gel:Alg = 2:1) and the incorporation of MPs exhibited reduced structural stability and increased filament sagging over unsupported spans (Fig. 5 and Fig. S7a). At a span of 4 mm, all Gel:Alg:MP formulations showed comparable deflection angles (~1.5°), indicating minimal susceptibility to collapse at short unsupported distances. At an 8 mm span, the 2:1:0 hydrogel displayed the largest deflection (9.0 ± 2.5°), whereas the 1:1:0 and 1:2:0 formulations exhibited substantially lower deflections of 2.5 ± 1.0° and 3.0 ± 1.0°, respectively (mean ± SD, n = 3). This trend became more pronounced at a 16 mm span, where the 2:1:0 formulation reached a deflection angle of 15.0 ± 2.5°, compared to 7.5 ± 2.0° and 6.0 ± 1.5° for the 1:1:0 and 1:2:0 groups, respectively. Notably, increasing the magnetic particle concentration within the 1:2:0 formulation, originally the least prone to collapse, led to a marked increase in deflection, approaching values observed for the 2:1:0 hydrogel. Among all the tested groups, the Gel:Alg:MP 1:2:0 composition maintained the best filament integrity across all gap distances. Furthermore, fusion tests demonstrated that all formulations replicated the CAD-defined inter-filament distances (Fig. S7b-d of the supplementary document). Quantitative analysis showed measured-to-theoretical filament width ratios of 2.4 ± 0.4 for the Gel:Alg:MP 1:1:0 formulation, 2.6 ± 0.5 for the 2:1:0 formulation, and 2.3 ± 0.5 for the 1:2:0 formulation, with statistically significant differences observed between the 1:1:0 and 1:2:0 groups

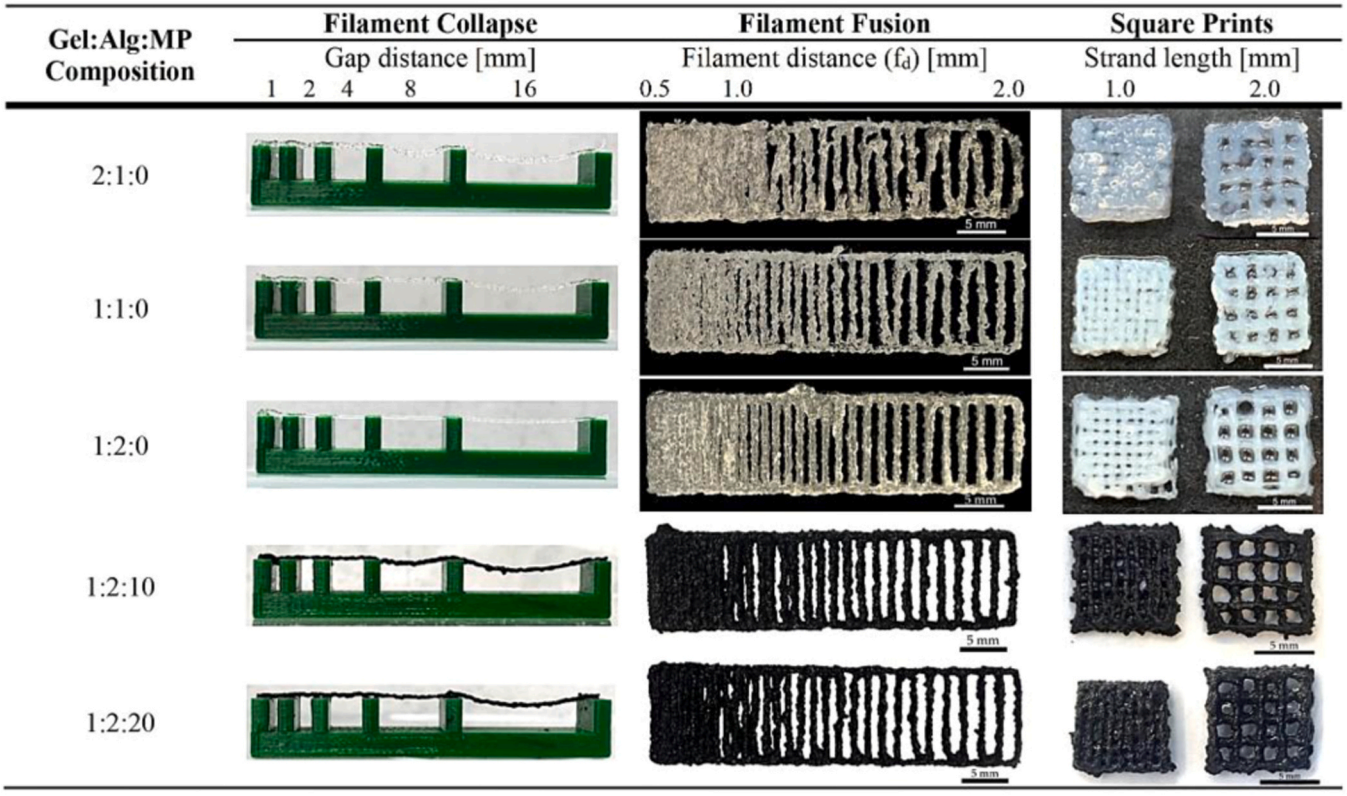

Fig. 5. Evaluation of hydrogel printability through filament collapse, filament fusion, and porous scaffold printing tests for various Gel:Alg:MP compositions.

($p < 0.05$). Incorporation of magnetic particles into the 1:2:0 hydrogel initially increased the filament expansion ratio to 2.5 ± 0.4 for the 1:2:10 composition. However, a further increase in the MP concentration to 1:2:20 reduced the filament width ratio to 2.1 ± 0.3, with a significant difference between these two magnetic formulations ($p < 0.001$). The observed filament widths, which were approximately twice the nozzle diameter, can be attributed to die swell, a well-known phenomenon in the extrusion of viscoelastic materials. During extrusion, elastic energy is stored in the polymer network under shear and pressure inside the nozzle and is rapidly released upon exit, leading to filament expansion. De Rosa et al. demonstrated pronounced die swell in viscoelastic bioinks due to elastic recovery after extrusion [34]. Similarly, Chai et al. quantified swelling ratios in sodium alginate-gelatin hydrogels and identified nozzle diameter as a dominant parameter governing filament expansion, arising from the instantaneous release of shear stress and pressure at the nozzle exit in such non-Newtonian fluids [35]. The 1:2:0 formulation exhibited the highest printing resolution and uniformity. Although the inclusion of MPs enhanced shape fidelity, it also resulted in thicker and bulkier filaments. High MP concentrations increased structural variability, leading to localized filament agglomerations.

Porous square scaffold prints. After 24 h of crosslinking, porous square scaffolds printed from the 1:2:0 formulation exhibited thinner and more uniform filaments than those from the 1:1:0 and 2:1:0 groups (Fig. 5). The addition of 10% and 20% MPs produced visibly bulkier filaments and reduced resolution, particularly evident in the diminished visibility of 1 mm pore gaps. At a 2 mm strand distance, post-crosslinking pores were smaller in the 1:2:20 group than in the 1:2:10 group, indicating that higher MP content affects both strand expansion and pore preservation.

3.3. Magnetic scaffold fabrication

The Gel:Alg:MP 1:2:0 multi-material scaffold (i.e., with and without red dye) displayed superior structural integrity and closer resemblance to the CAD model than the 1:1:0 composition (Fig. 6). The incorporation of MPs resulted in larger printed scaffold dimensions and reduced shrinkage after 24 and 48 h of crosslinking compared to MP-free scaffolds (Figs. 6 and 7). Initial tests with interlocking designs using varying unit cell dimensions are presented in Fig. S8 of the supplementary document.

Optical profilometry confirmed the predicted increase in surface roughness upon the inclusion of MP and application of a magnetic field. Due to significant topographical variation across the checkered design, roughness analysis was performed only on single-material scaffolds. The 1:2:10 and 1:2:20 formulations exhibited increased surface heights with

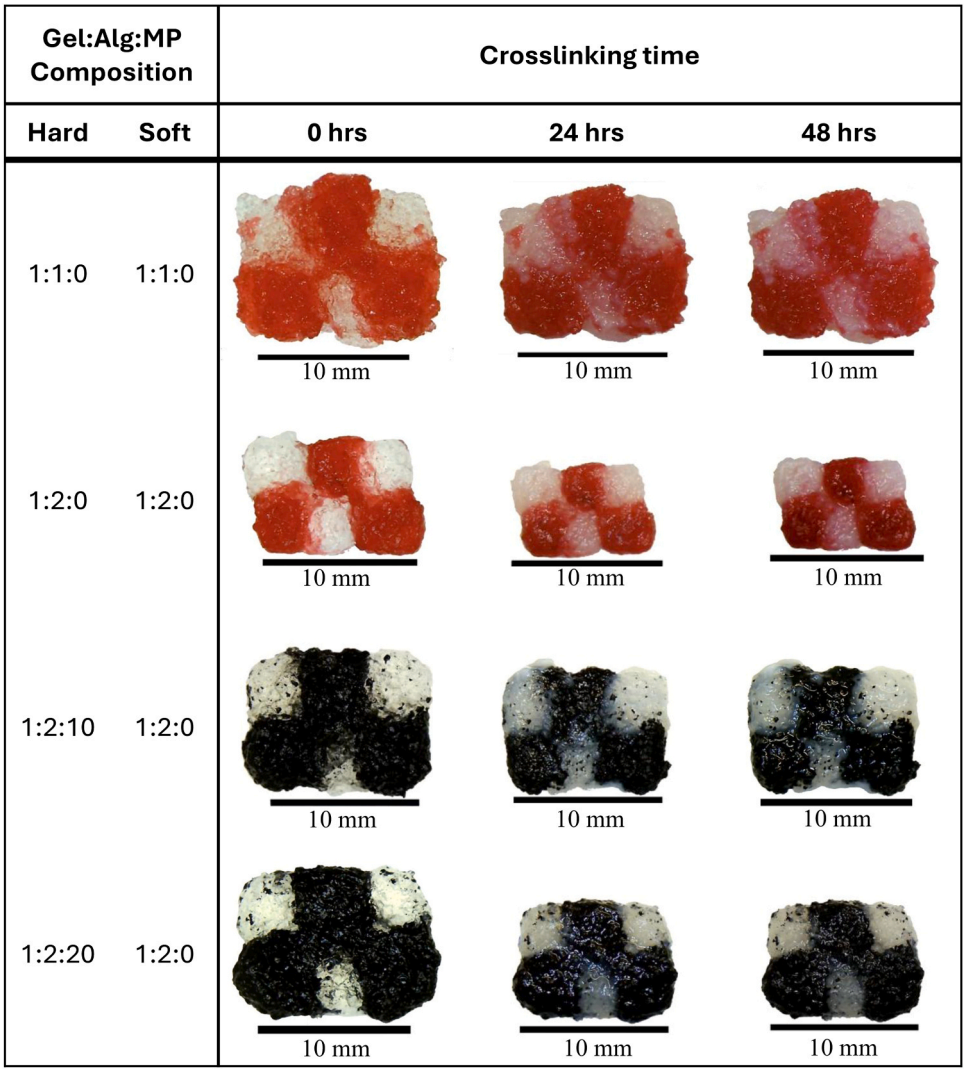

Fig. 6. Comparison of magnetic and non-magnetic hydrogel scaffold structures post-printing and at different crosslinking time points (0, 24, and 48 h). Rows indicate different material combinations for soft/hard regions: (1) 1:1:0 + 1:1:0, (2) 1:2:0 + 1:2:0, (3) 1:2:0 + 1:2:10, (4) 1:2:0 + 1:2:20.

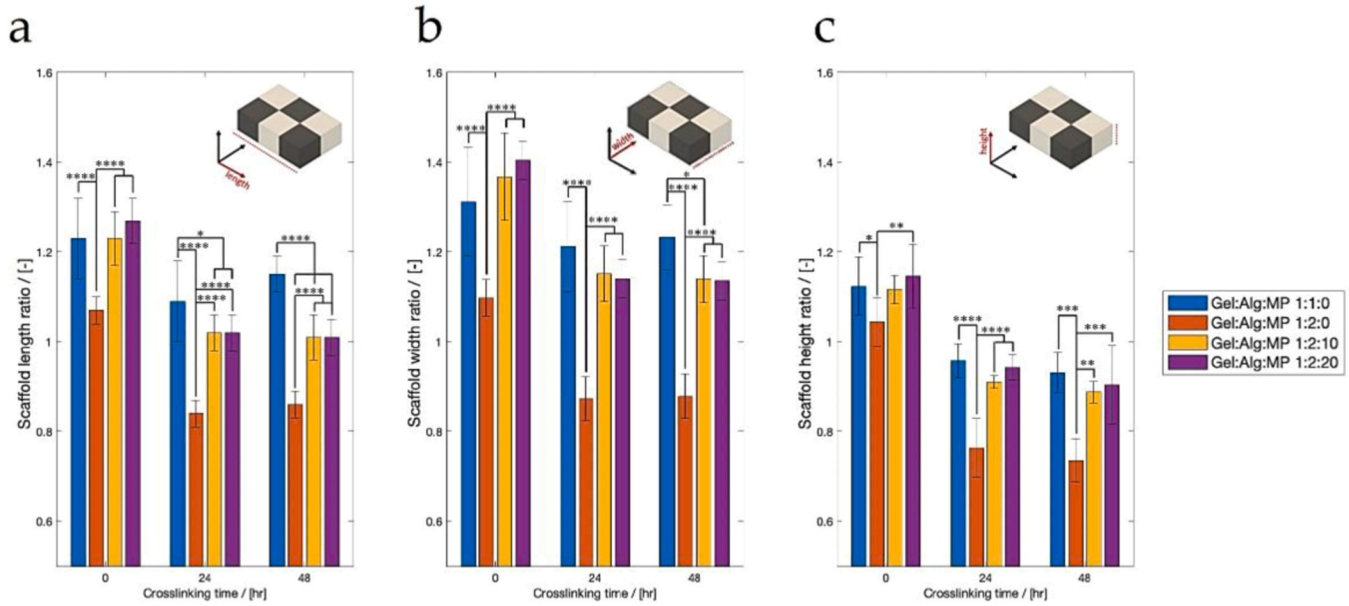

Fig. 7. Shape fidelity analysis in all 3 dimensions of the checkered multi-material scaffold design over a variety of crosslinking time points. Experimental/theoretical ratios of (a) length, (b) width, and (c) height are shown (mean ± SD). Statistical significance: $^{*}p < 0.05$, $^{**}p < 0.01$, $^{***}p < 0.001$, $^{****}p < 0.0001$; $n = 3$.

higher MP content, achieving arithmetic average roughness (Ra) values of 7.97 ± 1.51 μm and 8.76 ± 1.75 μm, respectively, in comparison to 5.02 ± 0.72 μm for the particle-free hydrogel (1:2:0). Statistical analysis confirmed significantly higher Ra values for both 1:2:10 and 1:2:20 relative to the control (1:2:0) ($p < 0.001$ for all comparisons). Additionally, Ra values differed significantly between the 1:2:10 and 1:2:20 groups ($p < 0.001$) (Table 1, Fig. S9 of the supplementary document). Upon application of magnetic stimulation, Ra decreased by 0.66 μm and 0.96 μm in the 1:2:10 and 1:2:20 formulations, respectively, indicating magnetically induced surface reconfiguration. Additionally, root mean square roughness (Rq) and the height range (maximum–minimum) are reported in Table 1.

3.4. Magnetic particle redistribution assessed by CT

Magnetic field–induced redistribution of MPs within the hydrogel scaffold was evaluated using μCT. Cross-sectional side-view μCT images acquired before and after magnetic field application are shown in Fig. 8a-b, together with the corresponding Y-axis center-of-mass histograms derived from segmented particle data.

Comparison of the reconstructed volumes further revealed a slight reduction in the overall dimensions of the hydrogel specimen after magnetic field exposure. Consistent with this observation, analysis of overlaid particle positions (Fig. 8c) indicated a uniform inward displacement of particles towards the scaffold center, with a mean center-to-center displacement of 84 ± 21 μm, reflecting modest, approximately isotropic contraction of the scaffold over time.

Table 1
Quantitative surface roughness parameters (mean ± standard deviation) obtained from profilometer measurements conducted on hydrogels Gel:Alg:MP 1:2:0, 1:2:10, 1:2:10 post-MAG, 1:2:20, and 1:2:20 post-MAG.

	Gel:Alg:MP				
	1:2:0	1:2:10	1:2:10 post-MAG	1:2:20	1:2:20 post-MAG
Ra ± Std. dev. (μm)	5.02 ± 0.72	7.97 ± 1.51	7.31 ± 1.33	8.76 ± 1.75	7.80 ± 1.49
Rq ± Std. dev. (μm)	5.07 ± 0.71	8.11 ± 1.54	7.43 ± 1.34	8.93 ± 1.77	7.94 ± 1.52
Range (μm)	9.26	17.52	18.05	16.82	15.52

In addition to this global contraction, quantitative analysis demonstrated a clear change in the particle distribution along the Y-axis (corresponding to the direction of magnetic field application) following magnetic field exposure. Distributional changes, quantified using the Kolmogorov–Smirnov distance (D_{KS}), exhibited a substantially larger distributional shift along the Y-axis ($D_{KS,y}$= 0.348) compared to the orthogonal axes ($D_{KS,x}$ = 0.057 and $D_{KS,z}$ = 0.134 for the X- and Z-axes, respectively). While small distributional differences were observed along the X and Z axes, the magnitude of the Y-axis redistribution was notably greater, indicating a direction-specific rearrangement of particles following magnetic field exposure. Particle distributions along the orthogonal axes remained comparatively similar before and after magnetization (Supplementary Fig. S10), consistent with the absence of preferential redistribution in those directions.

3.5. Mechanical and rheological characterization

3.5.1. Nanoindentation and material characteristics

The 1:2:10 formulation was identified as optimal for mechanical testing due to its consistent MP distribution, moderate surface roughness, and limited MP displacement during indentation. In contrast, the 1:2:20 formulation exhibited more pronounced MP movement, affecting measurement precision.

Viscoelastic behavior. The storage modulus of all single-material magnetic hydrogels was approximately twice the loss modulus, indicating an elasticity-dominant behavior (Fig. 9a–d). The addition of 10% MPs nearly doubled the storage modulus but led to a 20% decrease under a magnetic field, while the loss modulus remained stable. The damping factor analysis revealed a 75% reduction in energy dissipation after adding 10% MPs, followed by a 15% increase after magnetization. All formulations exhibited shear-thinning behavior, which is favorable for extrusion-based 3D printing (Fig. 9e). The addition of MPs showed a higher initial viscosity, 175 kPa·s, compared to the hydrogel composition without MPs, 95 kPa·s, which decreased during the application of a magnetic field and also post-magnetization to an intermediate level of 145 kPa·s.

Young's Modulus. The effective Young's modulus increased with MP addition and magnetic stimulation. For the Gel:Alg:MP 1:2:0, 1:2:10, 1:2:10 (with magnet), and 1:2:10 (post-magnet) specimens, average moduli were 90.96 ± 44.16, 159.29 ± 59.50, 172.05 ± 61.92, and

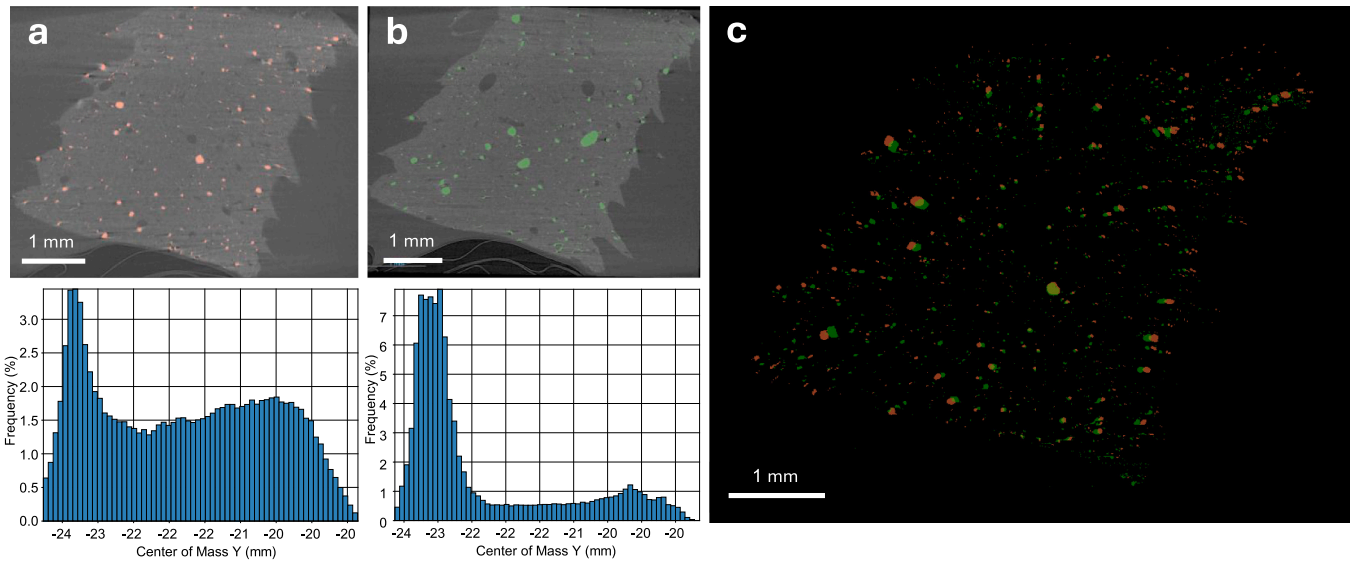

Fig. 8. The side-view μCT images of an iron-loaded hydrogel scaffold acquired (a) before and (b) after magnetic field application, with segmented MPs overlaid on the grayscale reconstruction (red: before, green: after). The corresponding Y-axis (direction of magnetic field application) center-of-mass histograms are shown below each image. (c) The overlay of segmented particle distributions before (red) and after (green) magnetic field exposure, illustrating the relative spatial arrangement of particles within the scaffold (Scale bars: 1 mm).

83.72 ± 34.81 kPa, respectively (Fig. 10a). Upon removal of the magnetic field, the modulus returned to beneath the baseline Gel:Alg:MP 1:2:10 levels, indicating reversible mechanical adaptation.

Multi-material scaffolds. The checkered, multi-material scaffolds exhibited a spatial transition in mechanical properties, from the stiffer 1:2:10 regions to the softer 1:2:0 zones (Fig. 9b and c). The application of a magnetic field resulted in a decrease in overall surface height, which returned to baseline after the field was removed. In the presence of a magnetic field, the Young's modulus of 1:2:10 regions did not increase further, while the softer 1:2:0 regions exhibited a noticeable stiffening effect (Fig. 10c). Post-field measurements revealed a decrease in elastic modulus across the scaffold, accompanied by increased variability in the 1:2:10 regions (Fig. 10d), indicating differential magneto-mechanical responses between the hard and soft domains.

3.5.2. Tensile integrity of biphasic constructs

Uniaxial tensile tests on homogeneous and biphasic hydrogel dogbone specimens were used to assess the mechanical integrity of the interface between magnetic and non-magnetic regions (Fig. 11a). Individual stress-strain curves are shown for both groups. Overall, biphasic specimens exhibited lower maximum stresses and strains at failure than homogeneous non-magnetic specimens, although considerable variability was observed within each group. Importantly, no abrupt stress drops indicative of premature interfacial failure were observed in the biphasic specimens prior to ultimate rupture. Quantitative analysis of the tensile response revealed that homogeneous hydrogel specimens exhibited an elastic modulus of 0.245 ± 0.092 MPa, whereas biphasic specimens showed a lower modulus of 0.186 ± 0.032 MPa. Similarly, the maximum stress and strain at failure were reduced in biphasic constructs (0.0598 ± 0.0148 MPa and 0.445 ± 0.175, respectively) compared to homogeneous specimens (0.155 ± 0.043 MPa and 0.95 ± 0.18).

In both homogeneous and biphasic specimens, failure occurred consistently within the neck region of the dogbone specimens rather than at the grip sections. For biphasic constructs, fracture did not occur at the interface between the magnetic and non-magnetic hydrogel regions, but instead at varying locations within the neck region, as observed visually after testing (Fig. 11b). No systematic interfacial delamination or separation between the two hydrogel phases was observed prior to or during failure.

3.6. In vitro cell viability

In vitro viability of preosteoblasts cultured on hydrogels without and with MPs (i.e., Gel:Alg:MP 1:2:0 and 1:2:10, respectively) was assessed using live/dead staining on days 1, 3, and 7 after seeding (Fig. 12).

The results indicated mostly viable cells on the Gel:Alg:MP 1:2:0 hydrogels at all time points (i.e., days 1, 3 and 7), with a corresponding increase in total cell number over the culture period. On the Gel:Alg:MP 1:2:10 hydrogels, fewer cells were observed at day 1, and a larger fraction of these cells appeared non-viable. However, both cell number and viability increased progressively with culture time. By day 7, both hydrogel formulations supported predominantly viable cells, although a slightly higher number of dead cells was observed on the iron-containing Gel:Alg:MP 1:2:10 hydrogels compared to the Gel:Alg:MP 1:2:0 controls.

3.7. Applications: bi-layered multi-material scaffolds

To mimic the stratified architecture and mechanical gradient of native osteochondral tissue, a bi-layered scaffold was fabricated, featuring a lower layer (6 × 4 × 2 mm^3) of Gel:Alg:MP 1:2:10 and an upper layer (6 × 4 × 4 mm^3) of Gel:Alg:MP 1:2:0 (Fig. 13a). A 210 μm nozzle was used to print the finer features of the layered construct. As observed in earlier tests, the 1:2:0 layer exhibited shrinkage after 24 h of crosslinking, resulting in minor geometric distortion. Upon sectioning, a distinct checkered interface was observed between the stiff (1:2:10) and soft (1:2:0) domains.

To explore broader applications, a disc-shaped scaffold was also fabricated, consisting of a softer inner core (Gel:Alg:MP 1:2:0) representing trabecular bone, and a stiffer outer ring (Gel:Alg:MP 1:2:10) simulating cortical bone (Fig. 13b, c). This demonstrates the tunability and versatility of the magnetic hydrogel platform in mimicking layered or region-specific mechanical environments, which is critical for osteochondral interface engineering.

4. Discussion

A central challenge in tissue engineering is the development of hydrogels that not only support cell growth but also promote differentiation, particularly at complex tissue interfaces. While magnetic hydrogels have demonstrated enhanced osteogenic and chondrogenic

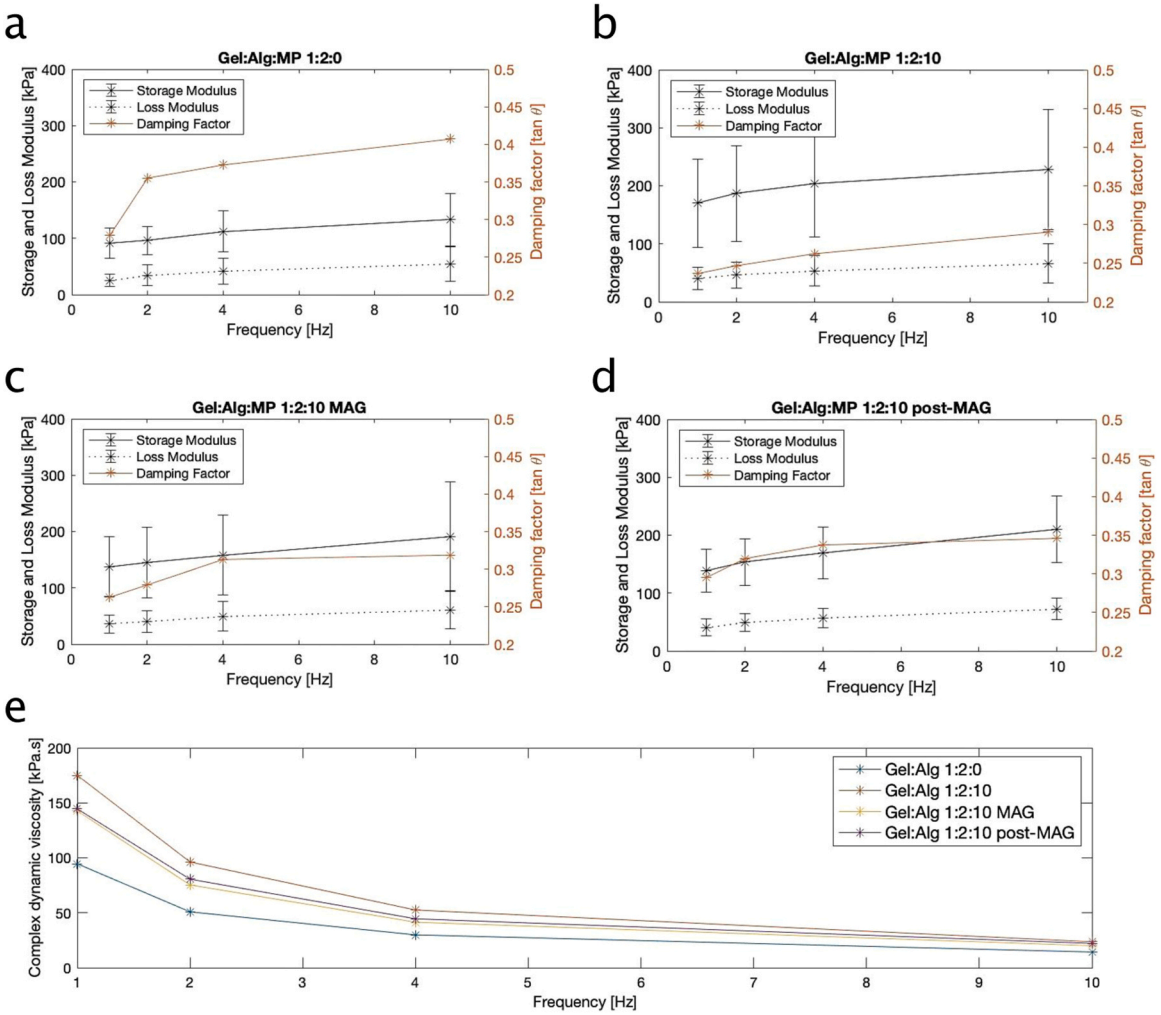

Fig. 9. Rheological characterization of Gel:Alg:MP hydrogels. Storage modulus, loss modulus, and damping factor for: (a) 1:2:0, (b) 1:2:10, (c) 1:2:10 under magnetic field (MAG), and (d) 1:2:10 post-magnetization. (e) Shear-thinning behavior evaluated via frequency-dependent dynamic viscosity (1–10 Hz). Data represent averages of $n = 3$.

differentiation in previous studies [21], their ability to support robust cell adhesion within hydrogel structures with the proper architectural and mechanical interfaces remains limited, primarily due to the lack of RGD peptide motifs in commonly used hydrogel systems which mainly make use of hydrogel structures of a single material. The 3D printability of hydrogels as well as the ability to integrate MPs within its polymer network gives us the potential to create advanced stimulus responsive materials [36]. In the present study, we created a structure with hard-soft interfaces with tuneable stiffness and increased interfacial adhesion that is needed for interface tissue engineering. This was achieved by formulating a 3D-printed, multi-material magnetic hydrogel architecture with spatially defined hard–soft interfaces based on gelatin and alginate, incorporating iron oxide MPs at specific locations to engineer hard-soft interfaces and enable tunable mechanical responses under an external magnetic field. The inclusion of gelatin introduced bioactive RGD sequences, intended to support cell attachment and better mimic the osteochondral microenvironment, which is known to be sensitive to mechanical stimuli. Moreover, our scaffold allowed for targeted stimulation through the combined magnetic actuation with quantitative structural and mechanical characterization, including μCT-based analysis of magnetic particle redistribution under an external field and nanoindentation to capture local stiffness changes at the microscale. This integrated approach provides mechanistic insight into how magnetic fields induce internal particle rearrangement and modulate non-contact scaffold mechanics.

In contrast to previously reported magnetic hydrogels based primarily on alginate-methylcellulose systems [22,23], the incorporation of gelatin in the present Gel:Alg formulation introduces bioactive RGD motifs into the hydrogel network, providing specific sites for cell adhesion and supporting cell-material interactions that are otherwise absent in purely polysaccharide-based matrices. This feature is particularly relevant for osteochondral applications, where cell attachment and phenotype regulation are critical.

Furthermore, by limiting the magnetic particle content to 10%, the present system avoids the increased brittleness, elevated extrusion pressures, and filament collapse reported at higher particle loadings in earlier magnetic hydrogel studies [22,23], while still achieving measurable magneto-responsive stiffening. Beyond material composition, the checkered multi-material and bi-layered architectures employed here enable spatially localized modulation of mechanical properties and provide a versatile design strategy for creating hard-soft interfaces. Such architectures can be extended to future scaffold designs to program spatial mechanical cues and enhance interfacial integrity across complex tissue interfaces. Overall, these features yield a biologically more relevant and mechanically tunable platform compared to existing magnetic hydrogel systems, particularly suited to osteochondral interface engineering.

Printability assessment. Hydrogel printability was evaluated through

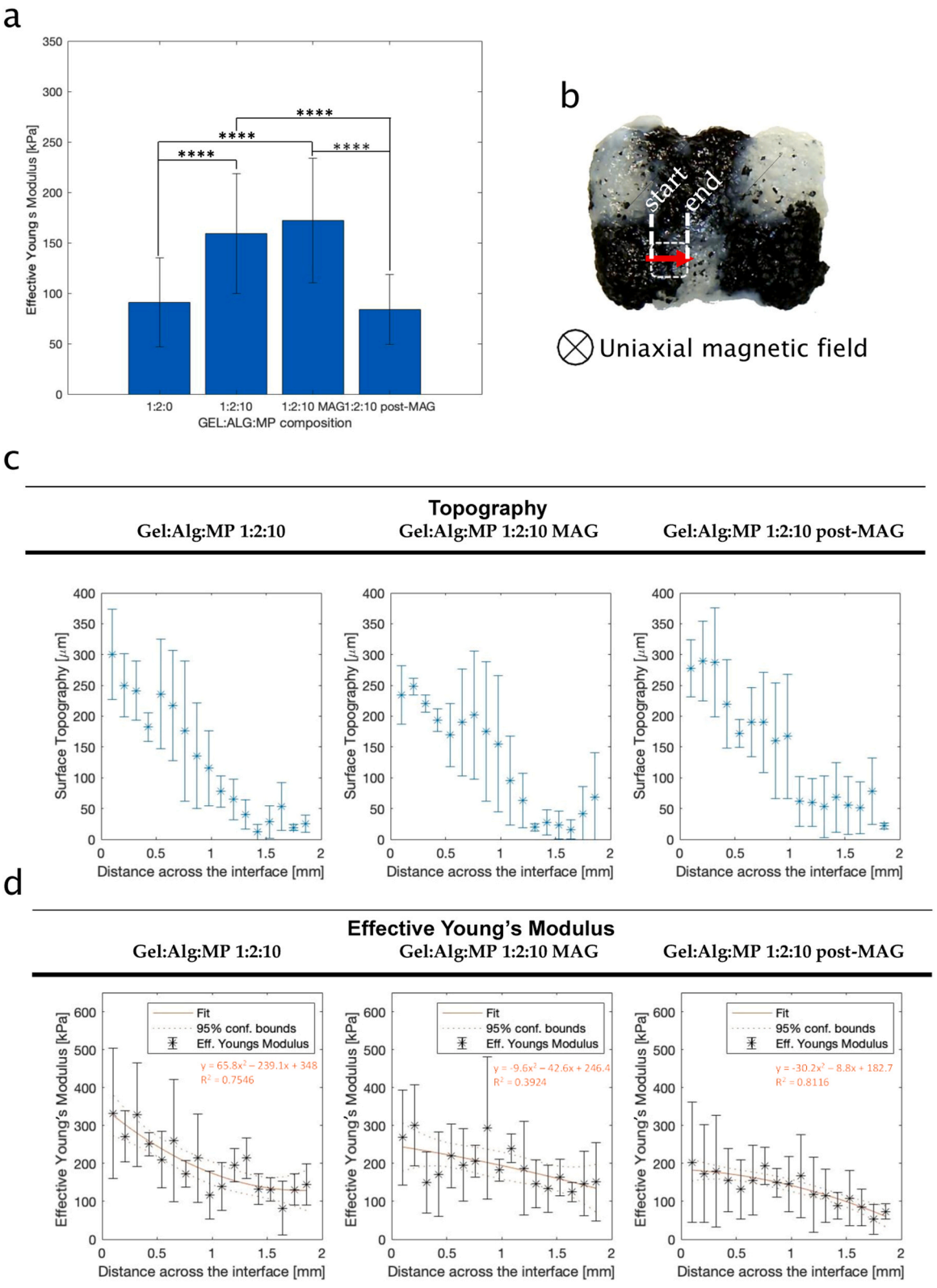

Fig. 10. (a) Effective Young's modulus of single-material scaffolds under different magnetic field conditions (mean ± SD, **** $p < 0.0001$; $n = 3$). (b) Example image of the 2 mm indentation path across hard-to-soft interface in multi-material scaffolds. (c) Surface topography and (d) spatial variation in Young's modulus across the hard–soft interface, with second-order polynomial fitting.

filament collapse and fusion tests. Consistent extrusion required continual adjustment of printing pressure, which was influenced by the hydrogel's viscoelastic properties and temperature sensitivity [37]. The addition of MPs increased filament sagging during printing, likely due to increased strand weight, which contributed to greater structural collapse at larger span lengths [21]. Filament fusion tests showed that the 1:2 Gel:Alg formulation yielded the best print resolution, attributed to a higher apparent ionic crosslinking between alginate and calcium

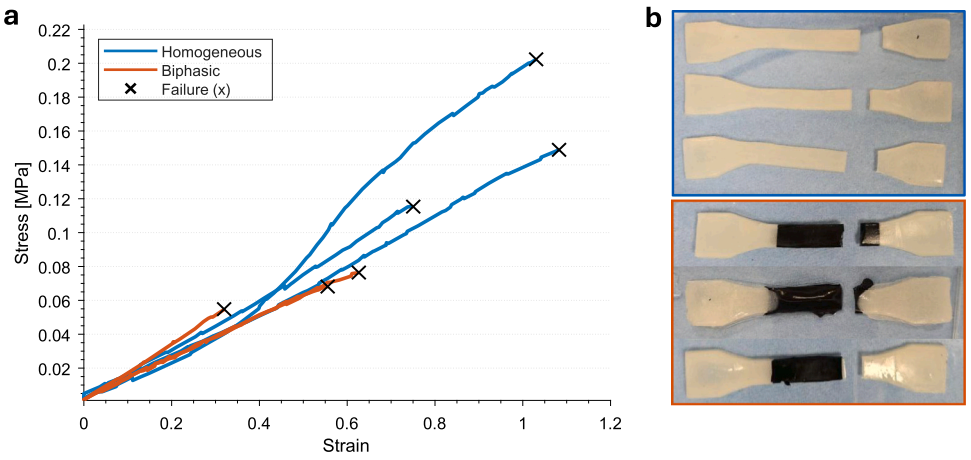

Fig. 11. The tensile integrity of homogeneous and biphasic hydrogel dogbone specimens. (a) Engineering stress-strain curves from individual uniaxial tensile tests of homogeneous non-magnetic hydrogels and biphasic hydrogels comprising spatially distinct non-magnetic and magnetic regions (n = 3 per group). Failure points are indicated by × symbols. (b) Representative photographs of homogeneous (top) and biphasic (bottom) hydrogel dogbone specimens after tensile testing, illustrating failure occurring within the neck region rather than at the interface between the hydrogel phases.

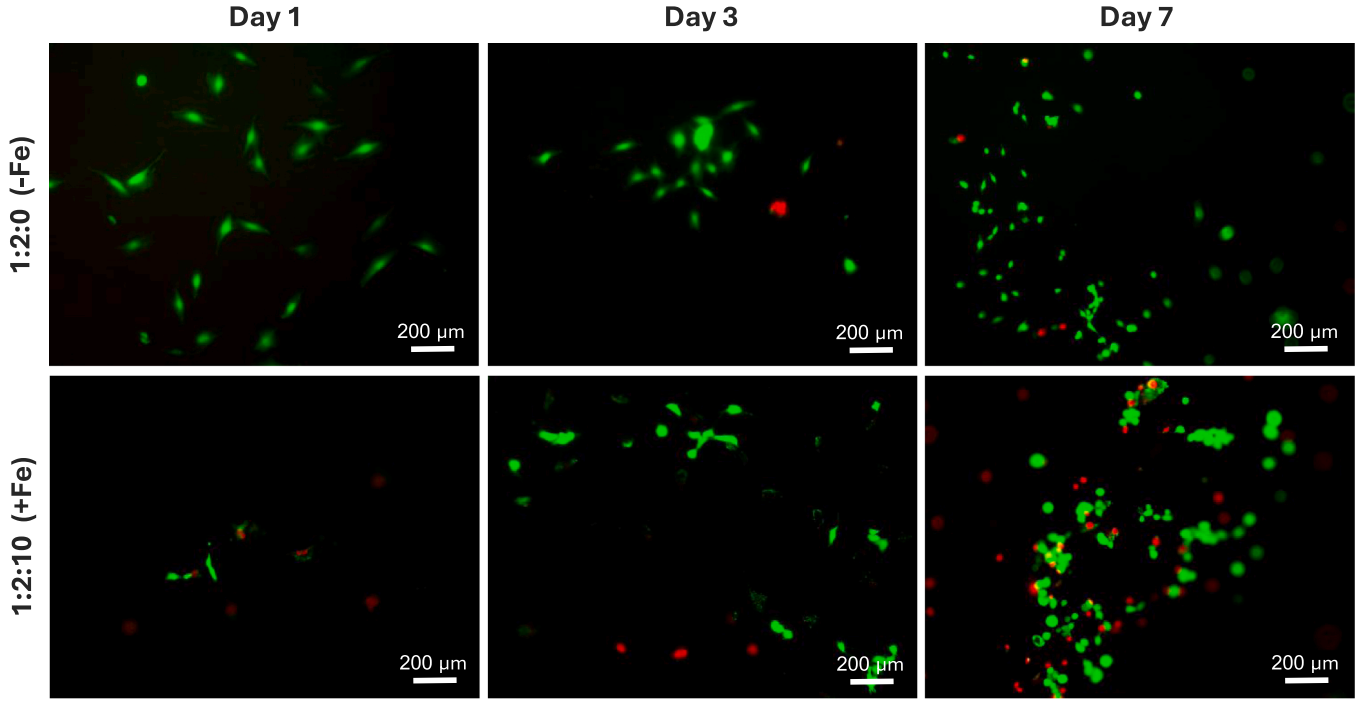

Fig. 12. Live/dead staining of preosteoblasts cultured on Gel:Alg:MP hydrogel discs with and without MPs. Representative fluorescence images were acquired on days 1, 3, and 7 after seeding for Gel:Alg:MP 1:2:10 (top row) and Gel:Alg:MP 1:2:0 (bottom row). Live cells are shown in green and dead cells in red (Scale bar: 200 µm).

ions due to the decrease in filament thickness and overall increase in filament uniformity, resulting in well-defined filaments aligned with the modeled distances (Fig. 5). Contrary to expectations, the inclusion of 10% MPs increased filament diameter, likely due to particle agglomeration and irregular flow through the nozzle. This not only reduced resolution but also increased surface roughness and variability. A potential strategy to mitigate magnetic particle-induced nozzle clogging and filament widening involves fine-tuning printing parameters such as print speed, extrusion pressure, and nozzle geometry. In particular, the use of larger nozzle diameters or nozzles with optimized taper angles may reduce shear-induced particle accumulation at the nozzle entrance. Moreover, lowering extrusion pressure and print speed can decrease local particle crowding and improve flow stability in particle-laden inks. Such parameter optimization strategies have been reported to reduce clogging and improve homogeneity of extrusion in composite bioinks [38]. Implementing these approaches may alleviate the widening effects observed at 10% MP content while preserving printability and functional performance.

Magnetic particle redistribution was assessed with CT. The µCT data indicate that the hydrogel scaffold underwent a modest, approximately isotropic shrinkage between the pre- and post-magnetization scans, leading to a uniform inward displacement of particles toward the scaffold center. Such shrinkage is consistent with time-dependent changes in hydrated polymer networks and, due to its isotropic nature, is not expected to substantially alter relative particle distributions along individual axes. However, quantitative distributional analysis revealed that

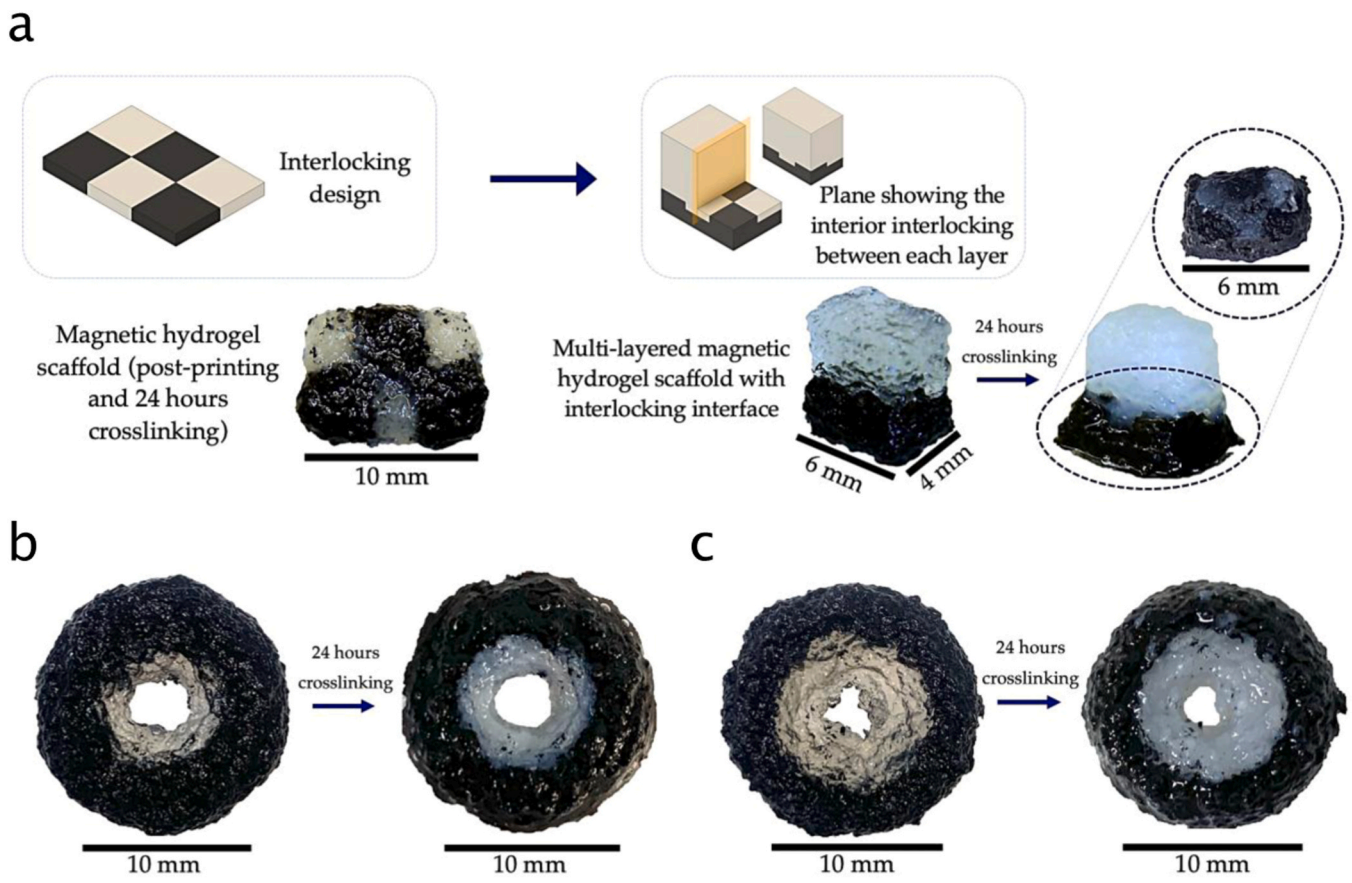

Fig. 13. Applications of the multi-material magnetic hydrogel scaffold: (a) Bi-layered scaffold (3.6 × 5.2 × 6 mm) composed of Gel:Alg:MP 1:2:10 (bottom) and 1:2:0 (top), mimicking the osteochondral interface. The inset highlights the checkered interface region. (b, c) Radially patterned constructs with 4 mm (b) and 5 mm (c) Gel:Alg:MP 1:2:0 inner discs surrounded by a Gel:Alg:MP 1:2:10 outer ring within a 12 mm diameter, simulating trabecular–cortical bone transition.

particle redistribution along the Y-axis (the direction of magnetic field application) was notably greater than along the orthogonal axes. The substantially larger distributional shift observed along the Y-axis exceeds what would be anticipated from uniform volumetric contraction alone, supporting the conclusion that the applied magnetic field contributed to directional particle migration within the scaffold.

The limited visibility of this effect in qualitative overlaid renderings suggests that magnetic actuation may preferentially influence smaller or more mobile particles, while larger particles remain constrained by the crosslinked hydrogel polymer network. This interpretation is consistent with the observation that pronounced distributional changes can be detected statistically even when macroscopic scaffold geometry remains largely preserved. Together, these observations suggest that magnetic fields can induce subtle but measurable internal rearrangements within hydrogel scaffolds while preserving overall structural integrity, even at highly crosslinked stages, an effect that may be advantageous for generating controlled internal gradients without macroscopic deformation.

Rheological and mechanical properties. The presence of MPs and their response to an external magnetic field significantly influenced the scaffold's rheological and mechanical properties (Figs. 8–10). MPs exhibited directional migration toward the magnetic source, which altered the local material stiffness. As the nanoindenter used a maximum indentation depth of 3 μm, even minor MP movement affected the mechanical response captured at the surface. The addition of MPs increased the effective Young's modulus from approximately 90 kPa to 160 kPa, further rising under magnetic stimulation (Fig. 10). Under a static magnetic field, viscous damping also increased, reflected in a higher damping factor and energy absorption capacity. However, stiffness did not fully revert to its pre-magnetization values after field removal, suggesting a semi-permanent rearrangement of MPs and changes in the local microstructure.

The hydrogel ink demonstrated shear-thinning behavior, which is favorable for extrusion-based printing. MP incorporation increased baseline viscosity, but viscosity decreased under magnetic stimulation, consistent with field-induced MP rearrangement that reduces internal resistance. All hydrogels underwent 24 h of crosslinking prior to rheological, mechanical, and printing characterization, resulting in solid-like behavior and preventing reliable steady-shear flow measurements without inducing sample fracture or slip. For this reason, we employed small-amplitude oscillatory measurements and applied the Cox-Merz empirical rule to estimate the apparent complex viscosity as a function of frequency. Notably, multi-material scaffolds subjected to prolonged magnetic exposure exhibited higher Young's moduli than single-material constructs, likely due to cumulative MP alignment and reinforcement over time.

Tensile tests: The tensile testing results show that biphasic hydrogels with magnetic and non-magnetic regions maintain mechanical continuity across the material interface. Although biphasic specimens exhibited lower maximum stresses and strains at failure compared to homogeneous non-magnetic hydrogels, fracture did not occur at the interface between the two phases. Instead, rupture consistently occurred in the neck region, indicating that the interface was not the mechanically weakest point of the construct. The absence of abrupt stress drops or interfacial delamination prior to failure further supports effective load transfer between the magnetic and non-magnetic hydrogel phases. Together, these findings suggest that mixing the two hydrogel formulations prior to crosslinking enables sufficient interfacial integration to sustain uniaxial tensile loading, and that the observed reduction in failure stress and strain in biphasic samples primarily stems from

differences in bulk material composition rather than inadequate interfacial bonding.

Cytocompatibility: The live/dead analysis indicates that incorporation of 10% MPs into the Alg:Gel:MP hydrogel does not adversely affect long-term cell viability of preosteoblast cells. While a reduced cell number and lower viability were observed on day 1 in the iron-containing hydrogels, this difference was transient and no longer apparent at later timepoints. By days 3 and 7, cell viability in Gel:Alg:MP 1:2:10 and Gel:Alg:MP 1:2:0 hydrogels was comparable, with both formulations supporting predominantly viable cells. The initial difference observed at early timepoints may reflect altered cell attachment, early adaptation to the iron-containing matrix, or local microenvironmental changes immediately following seeding, rather than sustained toxicity.

The absence of an increasing dead-cell signal over time suggests that incorporating 10% MPs into the Gel:Alg hydrogel does not induce delayed cytotoxic effects, thereby enabling the development of a magneto-responsive scaffold. The initial difference observed at early timepoints may reflect altered cell attachment, early adaptation to the iron-containing matrix, or local microenvironmental changes immediately following seeding, rather than sustained toxicity.

Methodological considerations. Mechanical property calculations were based on the Hertz contact model, which assumes linear elasticity, homogeneous and isotropic material behavior, and a parabolic indenter profile, among other idealized conditions [26,31]. Deviations from these assumptions, such as surface heterogeneity or localized MP clusters, could contribute to measurement variability [39]. Additional challenges included specimen movement and adhesion issues during indentation, highlighting the need for robust experimental protocols and careful interpretation of nanoscale mechanical data.

Outlook and future directions. The presented multi-material magnetic hydrogel scaffolds exhibit strong potential for osteochondral applications, particularly due to their interlocking checkered design, which may reduce delamination between soft cartilage and stiff bone regions. While the present study establishes mechanical tunability, interfacial integrity, and cytocompatibility, further biological validation, degradation behavior, swelling characteristics, and long-term MP-related cytotoxicity will be required to confirm osteochondral-specific functionality. Future work could incorporate bioactive ceramics, such as hydroxyapatite, to further enhance mechanical properties and stimulate osteogenic differentiation. The ability to dynamically modulate scaffold stiffness using external magnetic fields opens new areas for responsive biomaterial design.

Although cyclic magnetic stimulation is an important measure of durability in magneto-responsive systems, its applicability is limited in the present material design. The MPs used in this study were not surface-functionalized and therefore did not form chemical or physical bonds with the gelatin-alginate network, leading to irreversible particle displacement under a static magnetic field. After field removal, the effective stiffness did not recover to the pre-magnetization values, indicating irreversible structural rearrangement within the hydrogel. Under these conditions, repeated magnetic cycling would primarily reflect progressive particle migration rather than intrinsic material durability. Accordingly, reversibility was assessed once (1 h post-field removal) to evaluate remanent effects. This behavior represents an inherent design constraint of the current system and motivates future strategies based on particle surface functionalization or enhanced matrix-particle coupling to enable reversible and cyclic magneto-mechanical responses.

Further studies should explore the interplay between hydrogel printability, crosslinking mechanisms, mechanical loading, and cell behavior. Particular attention should be given to the kinetics of hydrogel degradation, spatiotemporal growth factor delivery, and the impact of magnetic fields on cellular organization and signaling. Collectively, these insights could accelerate the development of next-generation scaffolds for interface tissue engineering.

5. Conclusions

Beyond biomechanical, biochemical, and architectural tunability, the incorporation of localized MPs into hydrogel scaffolds offers a promising strategy for advanced tissue engineering applications, particularly in interface tissue systems that benefit from mechanical cues to drive cell differentiation. In this study, we developed and optimized a gelatin-alginate-based hydrogel containing iron oxide MPs, which was 3D printed to fabricate multi-material scaffolds featuring hard-soft interfacial regions.

The optimal hydrogel composition for extrusion was identified as 2.5% gelatin, 5% alginate, and 10% (w/v) MPs based on the printability results. This formulation exhibited magnetorheological behavior, characterized by an increase in the effective Young's modulus and a decrease in viscosity under a static magnetic field. CT data provided quantitative evidence of magnetic field-induced particle redistribution within the hydrogel, demonstrating that internal scaffold organization can be altered in a directional manner while preserving overall scaffold integrity. These tunable mechanical properties enabled the 3D printing of scaffolds with checkered architectures, establishing distinct regions of varying stiffness. Moreover, the bi-layered scaffold design introduced enhanced interfacial adhesion through the interlocking pattern, supporting structural integrity and functional layering. Furthermore, in vitro live/dead assays confirmed that the magnetic hydrogel system maintained cell viability, highlighting its suitability for biologically relevant applications. This multi-material magnetic hydrogel platform offers modularity and adaptability for replicating mechanically distinct tissue regions, such as the osteochondral interface, as well as create targeted regions that can be externally stimulated through magnetic field applications.

CRediT authorship contribution statement

E. Cinar San Segundo: Writing – original draft, Visualization, Validation, Methodology, Investigation, Formal analysis, Conceptualization. **L.B. Kunkels:** Writing – review & editing, Visualization, Validation, Methodology, Investigation, Formal analysis, Conceptualization. **S. Safarloo:** Writing – review & editing, Methodology, Investigation, Formal analysis, Data curation. **L. van Zanten:** Software, Methodology, Investigation, Formal analysis. **L.E. Fratila-Apachitei:** Writing – review & editing, Validation, Supervision, Methodology, Formal analysis. **A.A. Zadpoor:** Writing – original draft, Supervision, Resources, Investigation, Formal analysis. **M.J. Mirzaali:** Writing – original draft, Supervision, Resources, Project administration, Investigation, Formal analysis, Conceptualization.

Declaration of Competing Interest

The authors declare that they have no known competing financial interests or personal relationships that could have appeared to influence the work reported in this paper.

Acknowledgement

We are grateful to Prof. Dr. ir. Leon Abelmann and Dr. Iulian Dugulan for carrying out our vibrational sample magnetometry and Mössbauer spectroscopy experiments at their facilities at the Radiation Science & Technology Department of the Delft University of Technology.

Appendix A. Supporting information

Supplementary data associated with this article can be found in the online version at doi:10.1016/j.apmt.2026.103240.

Data availability

Data will be made available on request.

References

[1] P. Santos, S. Midha, A. Pitsillides, A. Miller, R. Torii, D. Kalaskar, Biofabrication of the osteochondral unit and its applications: Current and future directions for 3D bioprinting, J. Tissue Eng. 13 (Nov. 2022) 204173142211334, https://doi.org/10.1177/20417314221133480.

[2] J.W. Alford, B.J. Cole, Cartilage restoration, part 1: Basic science, historical perspective, patient evaluation, and treatment options, Am. J. Sports Med. 33 (2) (Feb. 2005) 295–306, https://doi.org/10.1177/0363546504273510.

[3] Arthritis in Color: Advanced Imaging of Arthritis, Am. J. Neuroradiol. 31 (1) (Jan. 2010) R1, https://doi.org/10.3174/ajnr.A1813.

[4] L. Zhou, V.O. Gjvm, J. Malda, M.J. Stoddart, Y. Lai, R.G. Richards, K. Ki-wai Ho, L. Qin, Innovative tissue-engineered strategies for osteochondral defect repair and regeneration: Current progress and challenges, Adv. Healthc. Mater. 9 (23) (2020) 2001008, https://doi.org/10.1002/adhm.202001008.

[5] J.F. Mano, R.L. Reis, Osteochondral defects: present situation and tissue engineering approaches, J. Tissue Eng. Regen. Med. 1 (4) (2007) 261–273, https://doi.org/10.1002/term.37.

[6] C.-C. Wang, K.-C. Yang, I.-H. Chen, Current treatment concepts for osteochondral lesions of the talus, Tzu Chi Med J. 33 (3) (Oct. 2020) 243–249, https://doi.org/10.4103/tcmj.tcmj_106_20.

[7] A.I. Caplan, Mesenchymal stem cells, J. Orthop. Res. 9 (5) (1991) 641–650, https://doi.org/10.1002/jor.1100090504.

[8] J. Xu, J. Ji, J. Jiao, L. Zheng, Q. Hong, H. Tang, S. Zhang, X. Qu, B. Yue, 3D printing for bone-cartilage interface regeneration, Front. Bioeng. Biotechnol. 10 (Feb. 2022), https://doi.org/10.3389/fbioe.2022.828921.

[9] J. Pak, J.H. Lee, N. Pak, Y. Pak, K.S. Park, J.H. Jeon, B.C. Jeong, S.H. Lee, Cartilage regeneration in humans with adipose tissue-derived stem cells and adipose stromal vascular fraction cells: updated status, Int. J. Mol. Sci. 19 (7) (July 2018), https://doi.org/10.3390/ijms19072146.

[10] Y. Cao, H. Zhang, M. Qiu, Y. Zheng, X. Shi, J. Yang, Biomimetic injectable and bilayered hydrogel scaffold based on collagen and chondroitin sulfate for the repair of osteochondral defects, Int. J. Biol. Macromol. 257 (Feb. 2024) 128593, https://doi.org/10.1016/j.ijbiomac.2023.128593.

[11] T. Gong, Z. Zhang, X. Liu, Y. Wang, J. Zhou, S. Wang, X. Liu, H. Jin, Z. Zhao, Microstructurally and mechanically tunable acellular hydrogel scaffold using carboxymethyl cellulose for potential osteochondral tissue engineering, no. Pt 1, Int J. Biol. Macromol. 253 (Dec. 2023) 126658, https://doi.org/10.1016/j.ijbiomac.2023.126658.

[12] W. Wang, H. Li, P. Song, Y. Guo, D. Luo, H. Li, L. Ma, Photo-crosslinked integrated triphasic scaffolds with gradient composition and strength for osteochondral regeneration, J. Mater. Chem. B 12 (5) (Jan. 2024) 1271–1284, https://doi.org/10.1039/d3tb02031b.

[13] A. Dimaraki, P.J. Díaz-Payno, M. Minneboo, M. Nouri-Goushki, M. Hosseini, N. Kops, R. Narcisi, M.J. Mirzaali, G.J.V.M. van Osch, L.E. Fratila-Apachitei, A. A. Zadpoor, Bioprinting of a zonal-specific cell density scaffold: a biomimetic approach for cartilage tissue engineering, Art. no. 17, Appl. Sci. 11 (17) (Jan. 2021), https://doi.org/10.3390/app11177821.

[14] F. Gao, Z. Xu, Q. Liang, H. Li, L. Peng, M. Wu, X. Zhao, X. Cui, C. Ruan, W. Liu, Osteochondral regeneration with 3D-printed biodegradable high-strength supramolecular polymer reinforced-gelatin hydrogel scaffolds, Adv. Sci. 6 (15) (Aug. 2019) 1900867, https://doi.org/10.1002/advs.201900867.

[15] C.P. Kruize, S. Panahkhahi, N.E. Putra, P. Diaz-Payno, G. van Osch, A.A. A. Zadpoor, M.J.J. Mirzaali, Biomimetic approaches for the design and fabrication of bone-to-soft tissue interfaces, ACS Biomater. Sci. Eng. 9 (7) (Nov. 2021) 3810–3831, https://doi.org/10.1021/acsbiomaterials.1c00620.

[16] W. Wang, R. Narain, H. Zeng, Chapter 10 - hydrogels, in: R. Narain (Ed.), Polymer Science and Nanotechnology, Elsevier, 2020, pp. 203–244, https://doi.org/10.1016/B978-0-12-816806-6.00010-8.

[17] D. Almeida, P. Sanjuan-Alberte, J. C. Silva, F.C. Ferreira, 3D (bio)printing of magnetic hydrogels: formulation and applications in tissue engineering, Int. J. Bioprint. 10 (1) (Aug. 2023), https://doi.org/10.36922/ijb.0965.

[18] E. Cinar SanSegundo, M.J. Mirzaali, L.E. Fratila-Apachitei, A.A. Zadpoor, Magnetized Cell-Scaffold Constructs for Bone Tissue Engineering: Advances in Fabrication and Magnetic Stimulation, Adv. Sci. 12 (4) (2025) e10094.

[19] M. Betsch, C. Cristian, Y.-Y. Lin, A. Blaeser, J. Schöneberg, M. Vogt, E.M. Buhl, H. Fischer, D.F. Duarte Campos, Incorporating 4D into bioprinting: real-time magnetically directed collagen fiber alignment for generating complex multilayered tissues, Adv. Healthc. Mater. 7 (21) (2018) 1800894, https://doi.org/10.1002/adhm.201800894.

[20] C. Czichy, D. Kilian, T.-C. Wang, S. Günther, A. Lode, M. Gelinsky, S. Odenbach, CyMAD bioreactor: a cyclic magnetic actuation device for magnetically mediated mechanical stimulation of 3D bioprinted hydrogel scaffolds, J. Mech. Behav. Biomed. Mater. 131 (July 2022) 105253, https://doi.org/10.1016/j.jmbbm.2022.105253.

[21] J. Spangenberg, D. Kilian, C. Czichy, T. Ahlfeld, A. Lode, S. Günther, S. Odenbach, M. Gelinsky, Bioprinting of magnetically deformable scaffolds, ACS Biomater. Sci. Eng. 7 (2) (Feb. 2021) 648–662, https://doi.org/10.1021/acsbiomaterials.0c01371.

[22] Y. Li, L. Huang, G. Tai, F. Yan, L. Cai, C. Xin, S. Al Islam, Graphene Oxide-loaded magnetic nanoparticles within 3D hydrogel form High-performance scaffolds for bone regeneration and tumour treatment, Composites Part A Applied Science Manufacturing 152 (Jan. 2022) 106672, https://doi.org/10.1016/j.compositesa.2021.106672.

[23] Y. Choi, C. Kim, H.S. Kim, C. Moon, K.Y. Lee, 3D Printing of dynamic tissue scaffold by combining self-healing hydrogel and self-healing ferrogel, Colloids Surf. B Biointerfaces 208 (Dec. 2021) 112108, https://doi.org/10.1016/j.colsurfb.2021.112108.

[24] Y. Tabata, A. Nagano, Y. Ikada, Y. Ikada, Biodegradation of hydrogel carrier incorporating fibroblast growth factor, Tissue Eng. 5 (2) (1999) 127–138, https://doi.org/10.1089/ten.1999.5.127.

[25] Z. Klencsár, Mössbauer spectrum analysis by evolution algorithm, Nucl. Instrum. Methods Phys. Res. Sect. B Beam Interact. Mater. At. 129 (4) (Sept. 1997) 527–533, https://doi.org/10.1016/S0168-583X(97)00314-5.

[26] J. Crangle, G.M. Goodman, The magnetization of pure iron and nickel, Proc. A 321 (1547) (Mar. 1971) 477–491, https://doi.org/10.1098/rspa.1971.0044.

[27] A. Ribeiro, M.M. Blokzijl, R. Levato, C.W. Visser, M. Castilho, W.E. Hennink, T. Vermonden, J. Malda, Assessing bioink shape fidelity to aid material development in 3D bioprinting, Biofabrication 10 (1) (Nov. 2017) 014102, https://doi.org/10.1088/1758-5090/aa90e2.

[28] D.C. Lin, D.I. Shreiber, E.K. Dimitriadis, F. Horkay, Spherical indentation of soft matter beyond the Hertzian regime: numerical and experimental validation of hyperelastic models, Biomech. Model Mechanobiol. 8 (5) (Oct. 2009) 345–358, https://doi.org/10.1007/s10237-008-0139-9.

[29] N. Antonovaite, M. Berardi, K. Bielawski, N. Rijnveld, Fiber-optics Based Nanoindenters for Studying the Mechanics of Diseases Oct. 2020 doi: 10.13140/RG.2.2.19720.85761.

[30] S.V. Beekmans, D. Iannuzzi, A metrological approach for the calibration of force transducers with interferometric readout, Surf. Topogr. Metrol. Prop. 3 (2) (Apr. 2015) 025004, https://doi.org/10.1088/2051-672X/3/2/025004.

[31] A.M. Smith, D.G. Inocencio, B.M. Pardi, A. Gopinath, R.C. Andresen Eguiluz, Facile determination of the Poisson's ratio and Young's Modulus of polyacrylamide gels and polydimethylsiloxane, ACS Appl. Polym. Mater. 6 (4) (Feb. 2024) 2405–2416, https://doi.org/10.1021/acsapm.3c03154.

[32] J. Cappello, V. d'Herbemont, A. Lindner, O. du Roure, Microfluidic in-situ measurement of poisson's ratio of hydrogels, Micromachines 11 (3) (Mar. 2020) 318, https://doi.org/10.3390/mi11030318.

[33] "ASTM D412 | Instron." Accessed: Feb. 04, 2026. [Online]. Available: ⟨https://www.instron.com/en/testing-solutions/astm-standards/astm-d412/⟩.

[34] S. De Rosa, D. Tammaro, G. D'Avino, Experimental and numerical investigation of the die swell in 3D printing processes, Micromachines 14 (2) (Feb. 2023) 329, https://doi.org/10.3390/mi14020329.

[35] W. Chai, Y. An, X. Wang, Z. Yang, Q. Wei, Optimization of SA-Gel hydrogel printing parameters for extrusion-based 3D bioprinting, Gels 11 (7) (July 2025) 552, https://doi.org/10.3390/gels11070552.

[36] J.K. Wychowaniec, D.F. Brougham, Emerging magnetic fabrication technologies provide controllable hierarchically-structured biomaterials and stimulus response for biomedical applications, Adv. Sci. 9 (34) (Dec. 2022), https://doi.org/10.1002/advs.202202278.

[37] A. Schwab, R. Levato, M. D'Este, S. Piluso, D. Eglin, J. Malda, Printability and shape fidelity of bioinks in 3D bioprinting, Chem. Rev. 120 (19) (Oct. 2020) 11028–11055, https://doi.org/10.1021/acs.chemrev.0c00084.

[38] Y.B. Pottathara, V. Kokol, Effect of nozzle diameter and cross-linking on the microstructure, compressive and biodegradation properties of 3D printed gelatin/collagen/hydroxyapatite hydrogel, Bioprinting 31 (June 2023) e00266, https://doi.org/10.1016/j.bprint.2023.e00266.

[39] J.D. Finan, P.M. Fox, B. Morrison, Non-ideal effects in indentation testing of soft tissues, Biomech. Model Mechanobiol. 13 (3) (June 2014) 573–584, https://doi.org/10.1007/s10237-013-0519-7.